

Top-Down Computational Design of Molecule Recognition Peptides (MRPs) for Enzyme-Peptide Self-Assembly and Chemiluminescent Biosensing

Lihong Yu, Chenglin Yang, Shuting Cheng, Qianqian Jiang, Yuehong Pang, and Xiaofang Shen*



Cite This: *Anal. Chem.* 2025, 97, 355–364



Read Online

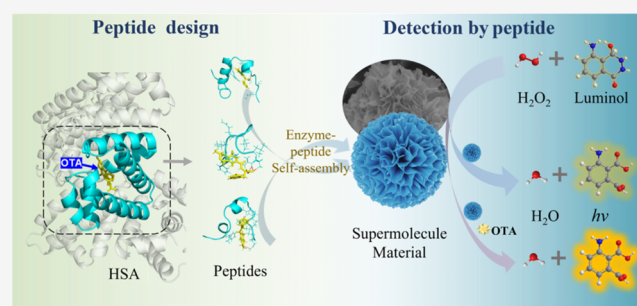
ACCESS |

Metrics & More

Article Recommendations

Supporting Information

ABSTRACT: The recognition of small molecules plays a crucial role in disease diagnosis, environmental assessment, and food safety. Currently, their recognition elements predominantly rely on antibodies and aptamers while suffering from a limitation of the complex screening process due to the low immunogenicity of small molecules. Herein, we present a top-down computational design strategy for molecule recognition peptides (MRPs) for enzyme-peptide self-assembly and chemiluminescence biosensing. Taking ochratoxin A (OTA) as an illustrative example, human serum albumin (HSA) was selected as the parental protein due to its high affinity for OTA binding. Through iterative computational simulations involving the binding domain of the HSA-OTA complex, our strategy identified a specific 15-mer MRP (RLKCASLKFGERAFK), which possesses excellent binding affinity (38.02 ± 1.24 nM) against OTA. Molecular dynamics simulations revealed that the 15-mer MRP unfolds into a flexible short chain with high affinity for OTA, but exhibits weak or no binding affinity with five structurally similar mycotoxins. Furthermore, we developed a novel enzyme-peptide self-assembly approach mediated by calcium(II) to obtain nanoflowers, which integrates both the recognition element (MRP) and the signal translator (enzyme) for chemiluminescence biosensing. The assembled nanoflowers allow MRPs to be directly utilized as a tracer for OTA biosensing without labeling or secondary antibodies. This computational-to-application approach offers a new route for small-molecule recognition.



INTRODUCTION

Small molecules serve as drugs, disease biomarkers, cell signaling molecules, and nutrients, yet they can also be toxic substances,¹ such as mycotoxins, pesticides, and plasticizers. Accurate recognition of these molecules is essential for many applications including physiological function research, disease diagnosis, environmental monitoring, and food analysis.² Currently, the recognition of small molecules in biosensing primarily relies on antibodies and aptamers, which demonstrate excellent affinity and selectivity in molecular recognition.^{3–456} However, antibodies produced by mouse monoclonal techniques and aptamers selected through systematic evolution of ligands by exponential enrichment (SELEX) require intricate screening processes and lengthy cycles, often lasting several weeks to months.^{1,7} Hence, the exploration of rapidly accessible molecular recognition elements is urgent to meet the increasing demand for novel tools for small-molecule identification.

Peptides, sharing the fundamental structural unit of antibodies, have the potential to serve as a protein receptor substitute. Unlike antibodies, peptides can be rapidly synthesized using standard Fmoc solid-phase peptide synthesis (SPPS) with customizable sequences and can be easily

modified at specific sites.^{8,9} Compared with aptamers, which are limited to four building blocks, peptides offer exponentially greater combinatorial diversity, allowing for more versatile targeting of different molecules. This means that even if the affinity of a parental peptide is moderate, it can be potentially increased by some computational evolution or structural activity studies. For example, the first hexapeptide for OTA was reported to have an affinity of 3.4×10^{-4} M.¹⁰ Subsequently, Rahi et al. reported a higher affinity peptide for OTA with $1.046 \mu\text{M}$ (K_d).¹¹ Designing small-molecule binders faces a challenge in enhancing binding affinities from micromolar to high nanomolar levels, and this limitation is not unique to OTA MRPs.

Currently, the screening of peptides capable of identifying small-molecule targets primarily utilizes phage display libraries.^{12–14} Phage display peptides have been used in the

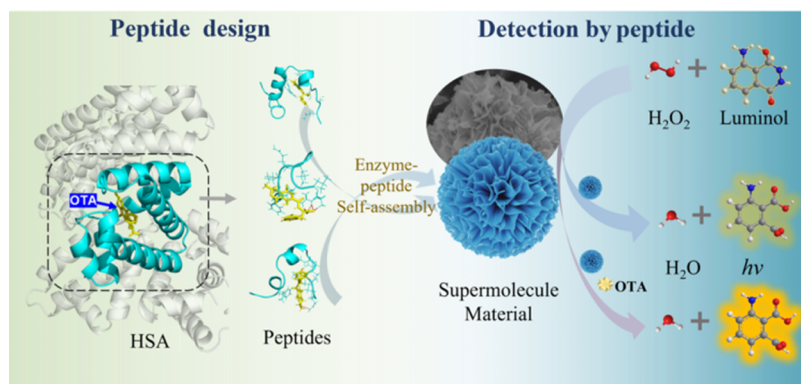
Received: August 12, 2024

Revised: November 10, 2024

Accepted: December 11, 2024

Published: December 20, 2024



Scheme 1. Schematic Illustration of the Proposed Computational Design of Molecule Recognition Peptides (MRPs) for Enzyme-Peptide Self-Assembly Biosensing

development of sensors for small molecules, such as ethyl carbamate,¹⁵ cadmium ions,¹⁶ and 2,4,6-trinitrotoluene (TNT).¹⁷ Despite the encouraging history of phage displays, the diversity of a library is constrained by the transformation efficiency, and the multiple rounds of selection for large libraries are very labor-intensive.¹² On the other hand, the computational design of MRPs is based on recapitulating the fundamental forces governing interactions between the ligand and the receptor, including van der Waals (vdW) forces, π - π interactions, and hydrophobic interactions.¹⁸ In the computational environment, peptides with different sequences, properties, and conformations can be designed for specific targets.^{19,20} The computational design for peptide screening offers advantages in terms of high efficiency, cost-effectiveness, repeatability, flexibility, and rich information content compared with experimentally screened methods. Depending on the target information and design objectives, the peptide design can range from top-down (template-based) to bottom-up (*de novo*).²¹ The top-down approach analyzes naturally occurring sequences of protein architecture to identify the most structurally important amino acids. The existence of a natural template for the top-down approach increases the possibility of successful peptide design, and the top-down approach has been applied to protein design.²² At present, a considerable amount of research has been undertaken regarding the computational design and detection application of macromolecules and particles.^{23–25} Designing macromolecule-targeting peptides is challenging due to their complex structures and multiple interactions, while small-molecule-targeting peptides are limited by fewer available interaction sites. This difficulty is particularly pronounced with polar small molecules, where hydrogen bonds formed between polar groups and water molecules make it even more challenging for MRPs to bind effectively.²⁶ Moreover, the designed peptide with a nanomolar binding affinity is necessary for achieving target recognition and sensitive detection.

Beyond binding, a general challenge is to transduce binding events into downstream signals. In many published studies, peptides have been used in the classical enzyme-linked immunosorbent assay (ELISA) instead of antibodies.²⁷ However, this method requires multiple washing steps and extended incubation times, failing to fully leverage the advantages of the MRPs' low molecular weight and ease of modification. In recent years, immobilized enzymes (inorganic-enzyme nanoflowers) have been used in ELISA for signal transduction due to the advantages of significantly enhanced

activity and stability.³¹ For biosensing, while immobilized enzymes enhance operability and catalytic efficiency, they do not streamline the sensing process. This limitation is also attributed to their single functionality. In parallel, we learned that peptides possess the remarkable ability to spontaneously trigger or self-assemble to form morphologically and structurally specific assemblies through hydrogen bonding, hydrophobicity, π - π stacking, and other noncovalent interactions.²⁸ The multivalency of peptides suggests that their bioactivities may be significantly enhanced when they are organized into supramolecular structures.²⁹ Furthermore, since peptides and enzymes share the same basic building blocks, the assembly process can effectively immobilize both functionalities simultaneously within the nanostructure. Therefore, the integration of peptides and enzymes through a coassembly facilitated by metal ions presents a new sensing strategy of peptide recognition. The method is expected to combine target recognition with signal transduction capabilities, thereby facilitating one-step biosensing.

In this work, we present a top-down computational design strategy for MRPs targeting small-molecule ochratoxin A (OTA), a naturally occurring carcinogenic mycotoxin that is widely distributed. We also propose an enzyme-peptide self-assembly approach to realize one-step chemiluminescence biosensing (Scheme 1). 15-mer MRPs were designed targeting OTA based on the OTA-binding domains in HSA. While HSA exhibits nonspecific binding and OTA, the specific amino acid sequence responsible for recognition can be isolated by extracting the key binding surface of the binding domain. The designed MRPs, which have low molecular weights, demonstrate high specificity for OTA and conformational matching with its structure. Additionally, by utilizing the stable and lightweight properties of peptides, a novel enzyme-peptide self-assembly technique was used to produce bifunctional assembled nanoflowers, enabling straightforward biosensing through enzyme-mediated translation of the binding signal between MRPs and small molecules in solution. This direct approach avoids using a conventional tool such as ELISA to detect receptor-target recognition. The study offers valuable insights into the design and application of MRPs in biosensing small molecules.

EXPERIMENTAL SECTION

HSA-Based MRP Design and In Silico Simulation. The molecule of OTA was docked to the protein using the AutoDock Vina program, aiming to identify the specific

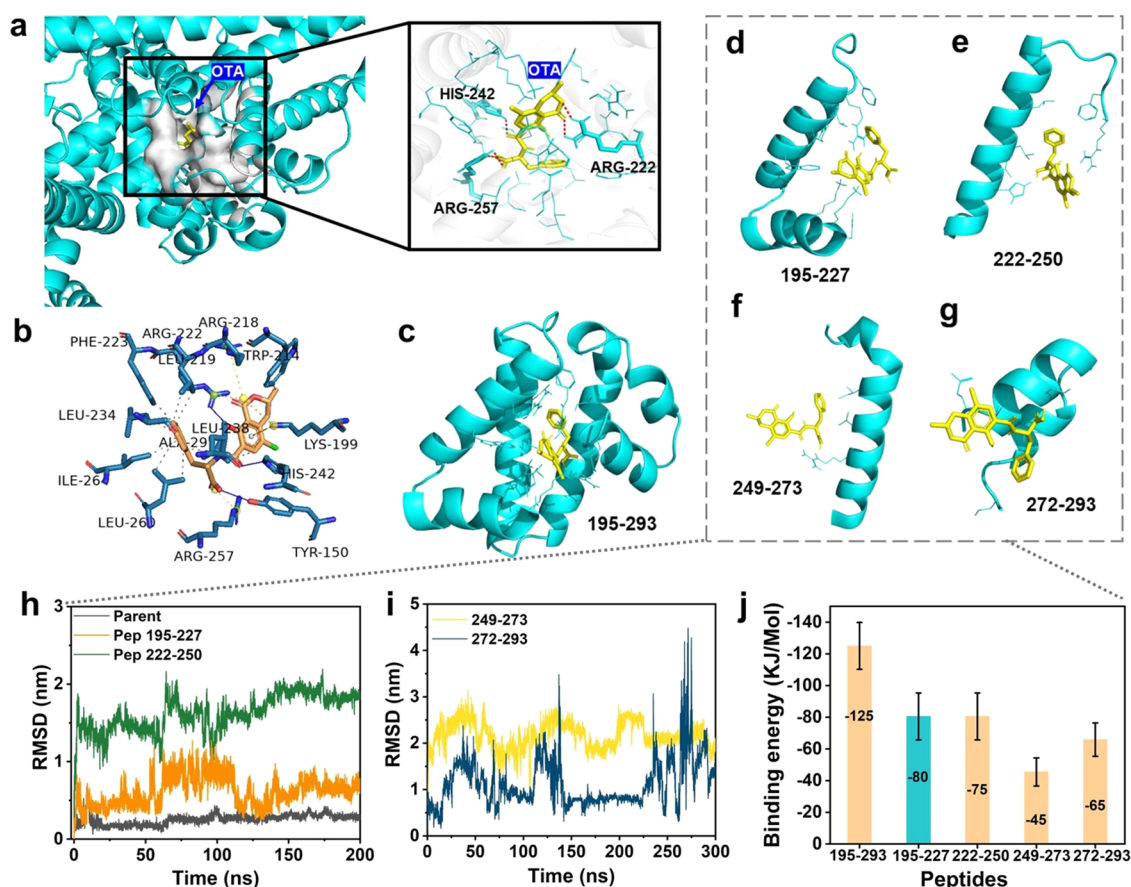


Figure 1. Construction of an HSA-based affinity peptide for OTA. (a) Binding site of OTA in HSA. (b) Noncovalent interaction of HSA and OTA analyzed by PLIP. (c) Parental peptide extract from HSA. (d–g) Four peptides derived from the parental peptide. (h, i) RMSDs of the different peptides-to-OTA following 200–300 ns simulations, the calculation mode of RMSDs from Gromacs is backbone to ligand. (j) Average interaction energies obtained during the final 10 ns were calculated utilizing the MM/PBSA method (the energies are reported in KJ/Mol).

binding site in Sudlow's site I of HSA. The crystal structure of HSA (1AO6) was downloaded from the RCSB Protein Data Bank (PDB) (<https://www.rcsb.org/>). OTA and its protonated structure were downloaded from the ZINC database (<https://zinc.docking.org/>). During the preprocessing stage of the protein, water molecules present within its crystal structure were removed, and subsequently, PDBQT files were produced utilizing the Autodock 1.5.6 Tools. The x , y , and z coordinates of binding sites used for docking were 31.649, 35.285, and 32.996, with a radius of 22.5 Å. The binding energy score was given as a standard to determine the best conformation of HSA and OTA.

MD simulations of all of the peptides with OTA were carried out in GROMACS (v.2022.3; <http://www.gromacs.org/>) with the CUDA accelerated. The DFT/B3LYP method with the 6-311 G** basis set was used to generate the ligand molecule in Gaussian 09 (C. 01), while the antechamber produced was used to fit the restrained electrostatic potential (RESP) charge. For detailed MD simulations methods and the calculation of the relative binding energy, please refer to the [Supporting Information](#).

Reagents. The peptides and biotin peptide were obtained from ChinaPeptides (Shanghai, China). Rhodamine B, horseradish peroxidase (HRP, ≥ 300 units mg^{-1}), luminol, *N*-hydroxysuccinimide (NHS), dicyclohexylcarbodiimide (DCC), and fluorescein isothiocyanate (FITC) were purchased from Aladdin (Shanghai, China). OTA standards were

purchased from Pribolab (Qingdao, China). The phosphate buffer solution was purchased from Sangon Biotech (Shanghai, China). All solutions were prepared by using ultrapure water sourced from Wahaha in Hangzhou, China. A certified reference material (whole wheat flour) obtained from Pribolab (Qingdao, China) was used for method validation.

Binding Assessment by Enzyme-Linked Peptide Assay. The microtiter plates were coated with $20 \mu\text{g}\cdot\text{mL}^{-1}$ OTA-BSA dissolved in 50 mM carbonate–bicarbonate buffer (pH 9.6) overnight at 4 °C. Subsequently, the plates were blocked with a casein blocking buffer for 2 h at room temperature. Biotin-labeled peptides (5–1000 nM) were then added and incubated at 37 °C for 2 h. After incubation, a high-sensitivity streptavidin-HRP conjugate (diluted 1:4000) was added to each well and incubated on a shaker at 37 °C for 30 min. Wells were washed with the phosphate buffer solution containing 0.5% Tween 20, followed by the addition of 3,3',5,5'-tetramethylbenzidine (TMB) and incubation at 37 °C for another 30 min. The absorbance was measured at 450 nm using a microplate reader (Synergy H1, BioTek) after the addition of 2 M H_2SO_4 . Binding saturation curves and dissociation constant (K_d) values were fitted using GraphPad Prism 10 software using the equation $Y = B_{\text{max}} \cdot X / (K_d + X)$, where Y represents the absorbance value at various concentrations of 15-PEP, B_{max} corresponds to the maximum absorbance value in the fitted curve, and X represents the concentration of 15-PEP.

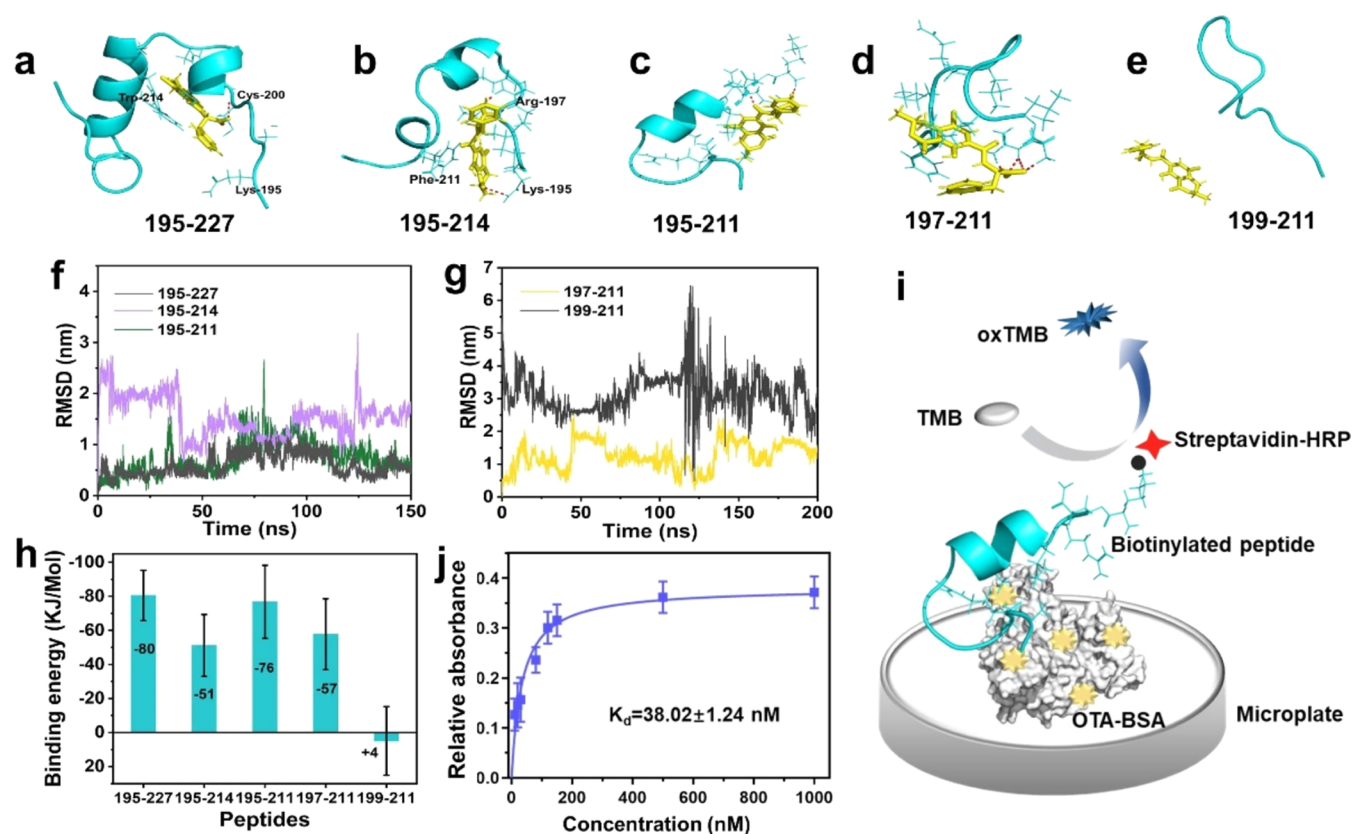


Figure 2. MD simulation of the peptide and OTA. Final conformations of peptides (a) 195–227, (b) 195–214, (c) 195–211, (d) 197–211, and (e) 199–211 showing the interactions with OTA. (f, g) RMSDs of the peptide and OTA complexes following 150–200 ns simulations. (h) Average interaction energies obtained during the final 10 ns were calculated utilizing the MM/PBSA method. (i) Schematic illustration of the binding assessment by enzyme-linked peptide assay. (j) Binding saturation curve and K_d value of 15-PEP fitted by GraphPad Prism.

Preparation of Peptide Nanoflowers and the Reaction System. Peptide nanoflowers (PNFs) were synthesized by self-assembly at room temperature, referring to the method of other hybrid nanoflowers previously published.^{30,31} To be specific, 250 μL of HRP (2 $\text{mg}\cdot\text{mL}^{-1}$) and 250 μL of the 15-mer peptide (30 $\text{mg}\cdot\text{L}^{-1}$) were added into 1 mL of the phosphate buffer solution (5 $\text{mmol}\cdot\text{L}^{-1}$, pH 7.4) in 2 mL tubes. After the mixture was mixed, the key to form crystal nuclei of CaCl_2 (20 μL , 200 $\text{mmol}\cdot\text{L}^{-1}$) was added. And the nanoflowers without peptides (NFs) were prepared in the same way. After 18 h reaction time, the nanoflowers were purified by centrifugation at 10,000g for 5 min. Then, the nanoflowers were washed six times with ultrapure water consecutively, until the supernatant no longer turned blue upon reacting with TMB, indicating that all free HRP was completely removed. Finally, PNFs and NFs were obtained and dried in a vacuum freeze-dryer for about 24 h. They were then resuspended in 1 mL of ultrapure water by vortexing while using.

50 μL of PNFs were first added to the white 96-well assay plate, and then different concentrations of the OTA standard solution or the sample extract solution in water (containing 1% (v/v) acetonitrile) were added to the wells. After 2 min, a luminous solution (containing 5 $\text{mmol}\cdot\text{L}^{-1}$ luminol at pH 12 and 15 mM H_2O_2 , 100 $\mu\text{L}/\text{well}$) was introduced. Subsequently, the chemiluminescence (CL) intensity was measured using a multimode microplate reader (Cytation 3, BioTek, VT).

Pretreatment of Grain Samples. Multiple different samples were obtained from local areas, including wheat, white and yellow maize, oats, and beer, and the grains were placed in a humid environment for 2 weeks. The samples were processed in accordance with the Chinese National Food Safety Standard (GB 5009.22–2016), with the inclusion of additional saponification steps to minimize the presence of oils in the grain extract solution, thereby mitigating the potential interference with the determination of CL. Briefly, grain samples were finely ground, and then 5.0 g of powder was extracted with 10 mL of acetonitrile/water (6:4, v/v) solution containing 0.5 g of NaCl. After 30 min of ultrasonic-assisted processing, the solutions were centrifuged at 8000g for 10 min and the supernatant was retained. Then, 0.5 g of NaOH was added and left for 10 min; the mixture was centrifuged again, followed by the supernatant. The certified reference material (whole wheat flour) was treated in the same way. The beer was first degassed by an ultrasonic treatment of 30 min. Following this, 2% NaHCO_3 solution containing 15% NaCl (m/z) was added, and the resultant mixture was filtered until achieving clarity. Prior to detection, all of the extracting solutions were filtered using a 0.22 μm filter membrane. An 8-fold dilution was made with deionized ultrapure water prior to analysis.

RESULTS AND DISCUSSION

Design Affinity MRPs for OTA with a Top-Down Strategy. Upon entering the human body, over 99.8% of circulating OTA forms a noncovalent bond with human serum albumin (HSA) due to its exceptionally high affinity.^{32–34}

Thus, HSA was selected as the parental protein for OTA and a top-down strategy was adopted to design the MRPs. Based on the crystal structure of HSA (PDB: 1AO6) and the structure of OTA obtained from ZINC (zinc.docking.org), we initially analyzed the OTA-binding domains of HSA using AutoDock. This analysis has identified the binding site with the highest affinity, located in Sudlow Site II of subdomain IIA of albumin, which forms a centrally hydrophobic cavity (Figure 1a). It is consistent with the literature report³⁵ and it was found that bound OTA exists in a dianionic form. Subsequently, the noncovalent interaction between the protein and OTA was analyzed using a protein–ligand interaction profiler (PLIP),³⁶ revealing the formation of a hydrogen bond network involving key residues, namely, 150 (Y), 199 (K), 214 (W), 218 (R), 219 (L), 222 (R), 223 (F), 234 (L), 238 (L), 242 (H), 257 (R), 260 (L), 264 (I), and 291 (A) (refer to Figure 1b). Hence, the fragment encompassing all of the above residues, with the exception of residue 150 located distantly in another α -helix termini, was extracted (the long peptide of 195 to 293) (Figure 2c). To identify the specific lightweight peptides, the parental peptide (195 to 293) was divided into four separate peptides for individual simulations (Figure 1d–g). These four peptides correspond to residues 195–227 (Figure 1d), 222–250 (Figure 1e), 249–273 (Figure 1f), and 272–299 (Figure 1g), all of which maintained their nativelike α -helical structure as intact as possible. Long peptides, as depicted in Figures 1d–g, contain repetitive amino acids at both the initial and final positions, which serve the purpose of preventing the omission of crucial amino acids during the acquisition of shorter peptides. The specific sequences of these peptides can be found in Supplementary Table S1.

To investigate the binding conformations and binding affinities to OTA, molecular dynamics (MD) simulations of peptides binding to OTA were conducted in a solvent environment to obtain a dynamic perspective at the single molecular level. Initially, the parental peptide (residues 195–293) and four long peptides-to-OTA were simulated, respectively; the root-mean-square deviation (RMSD) fluctuations of peptides and the OTA complex over a duration of 200 ns are shown in Figure 1h,i (the RMSDs were calculated by the peptide opposite OTA by Gromacs), and the RMSDs of only peptides (backbone) is shown in Figure S1. And the structure of the complex after MD is shown in Figure S1. It is evident that the RMSD of the parental peptide (Gray) exhibits fluctuations of less than 0.1 nm after 25 ns and subsequently remains stable throughout the entire 200 ns simulation. The final 10 ns trajectory was extracted to calculate the binding energy using MM/PBSA, revealing an average binding energy of -125 KJ/Mol between the parental peptide and OTA (Figure 1j). This evidence strongly suggests that the parental peptide from the binding domain forms a stable binding with the OTA molecule, indicating its potential utility in the design of more compact MRPs. The four truncated peptides from the parental peptide, specifically the peptides of 195–227 and 222–250, display minimal fluctuations (Figure 2h,i) and reach a plateau in the last 50 ns (Figure 1h, blue). Moreover, the RMSD of the backbone (only peptide) also shows similar stability; the whole MD simulation in 200 ns exhibits fluctuations of less than 1 nm (Figure S2). Additionally, the average binding energy of -80 and -75 KJ/Mol is lower than those of other peptides (Figure 1i). As such, peptides 195–227 and 222–250 were chosen as potential candidates for subsequent truncation in order to obtain a shorter affinity

peptide for small-molecule OTA. From Figure 1h, we can also observe that compared with peptide 222–250, the RMSD of peptide 195–227 shows less fluctuation (0–1 nm). Due to the little difference in the binding energy between the two and OTA, we speculated that 195–227 was more stable than 225–250 combined with OTA.

Short Affinity MRP Obtained Based on the Conformation Analysis and Binding Energy. Although 195–227 is considered the most potential long peptide to design the lightweight MRPs, we first try to evaluate the short peptides 222–235 and 236–250 extracted from 222 to 250, which exhibited a consistent and smooth fluctuation (1–2 nm) in RMSD at the last 50 ns (Figure S3). However, it was observed for the two short peptides that the binding energy exceeded zero, suggesting a lack of affinity (Figure S4). Peptide 195–227 comprised a total of 33 residues, and in an effort to minimize the difficulty and expenses of synthesis, we assessed the interaction between peptide 195–227 and OTA and devised a number of truncated peptides based on these findings. Subsequently, MD simulations lasting 100–300 ns were conducted. The final conformations of peptide 195–227 and various truncated peptides derived from the 195–227 region in water simulations are depicted in Figure 2a–e. It can be seen in Figure 2a that the latter half (215–227) of peptide 195–227 does not exhibit any direct interaction with OTA, while the crucial residues that interact with the ligand are concentrated in the range of 195–214. Notably, a hydrogen bond is formed between Cys-200 and OTA, playing a key role in the stable binding of the peptide–OTA complex. Consequently, peptide 195–214 was picked for further simulation. As shown in Figure 2b, 200 ns long simulations revealed that peptide 195–214 deforms from the C-terminal, especially the last three residues (212, 213, and 214) moving away from the OTA-binding region. Therefore, we next selected the peptide 195–211 and then attempted to remove residues from the N-terminal-obtaining peptides 197–211 and 199–211. As shown in Figure 2c–e, 150–200 ns long simulations demonstrated that peptides 195–211 and 197–211 maintained a stable binding to OTA, whereas peptide 199–211 exhibited occasional dissociation of the ligand in certain frames.

To further quantify the binding of these peptides to OTA, the time evolution of RMSDs and the binding energies of peptides and OTA were calculated and are presented in Figure 2f–h. Unexpectedly, the RMSD of 195–211 fluctuated smoothly (Figure 2f) and exhibited a stronger binding affinity (-76 KJ/Mol, Figure 2h) compared to peptide 195–214. This can be attributed to the more complete unfolding of the α -helix after removing the three tail residues. Although peptide 197–211 shows a slightly larger fluctuation in RMSD, none of the data points exceeded 2.5 nm and eventually reached a plateau. After 200 ns simulations, the original α -helix structure of this peptide, consisting of included 15 residues, underwent complete unfolding. Consequently, a long and flexible chain was formed, which enveloped the OTA molecule. Moreover, the number of H bonds formed by the protein with the ligand molecules was calculated and is depicted in Figure S5. And the binding energy was -57 KJ/Mol, indicating a high binding affinity to OTA. In contrast, peptide 199–211 exhibited significant fluctuations in RMSD, consistent with its previous conformation depicted in Figure 2e. Furthermore, it displayed a weak binding affinity of $+4$ KJ/Mol, as shown in Figure 2h. Considering both the binding affinity and the number of residues, peptide 197–211 (referred to as 15-PEP) was

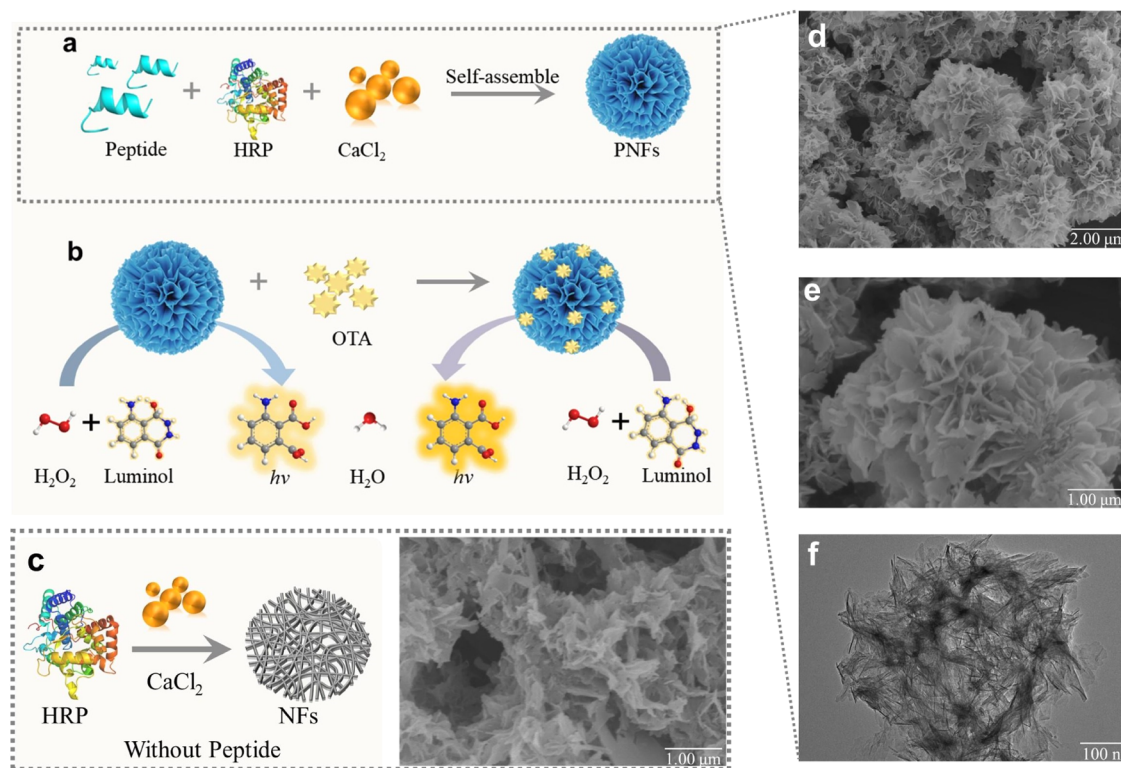


Figure 3. (a) Preparation process of PNFs. (b) Schematic diagram of the detection of OTA by CL using PNFs. (c) Schematic diagram and morphology of the nanoflowers without peptides during self-assembly. (d) SEM images and (e) locally enlarged images of PNFs. (f) TEM images of PNFs. Scale bars are shown in the diagram.

selected as the OTA-binding MRP for further investigation. The sequence of 15-PEP is RLKCSALKFGGERAFK.

MD Simulations of 15-PEP with Structurally Similar Mycotoxins. We have obtained affinity MRP (15-PEP) based on the OTA-binding domain within HSA. The analysis of synthesized 15-PEP is shown in Figure S6. To assess 15-PEP relative specificity, the 100 ns MD simulations were conducted for 15-PEP to several structurally similar mycotoxins, including aflatoxin B1 (AFB1), fumonisin B1 (FB1), patulin (PAT), deoxynivalenol (DON), and zearalenone (ZEN). The RMSDs of the backbone to ligand and binding energies of last 10 ns were calculated to evaluate its binding stability and affinity. Figure S6 demonstrates that only AFB1 exhibited a brief period of stability in the RMSD from 30 to 50 ns, but this stability is not sustained and is accompanied by notable fluctuations. Additionally, the RMSDs of the other four mycotoxins all fluctuated wildly, indicating that these mycotoxins with 15-PEP hardly form a stable conformation and a valid bond. That was consistent with the calculated binding energy >0 KJ/Mol (Figure S7), suggesting that these structurally similar mycotoxins exhibit weak or no binding affinity with 15-PEP. These results further indicate that 15-PEP designed from the OTA-binding domain shows distinct specificities.

Binding Affinity Assessment of 15-PEP and OTA by Enzyme-Linked Peptide Assay. The binding affinity was determined by enzyme-linked peptide assay, and the schematic diagram is shown in Figure 2i. The binding saturation curve is shown in Figure 2j, and the R^2 value obtained for the linear curve was 0.98. Binding affinity tests to BSA as a control are shown in Figure S9. The dissociation constant (K_d) value was obtained using quadratic fits and is shown 38.02 ± 1.24 nM,

which are significantly higher than previously reported binding peptides for OTA.^{10,11,27} The result further demonstrated the potential of 15-PEP for OTA sensing application.

Design and Construction of the Enzyme-Peptide Self-Assembly Supermolecule Material. In order to realize the one-step detection of OTA and make full use of the advantages of lightweight peptides, the enzyme-peptide self-assembly technique was developed to create bifunctional assembled peptide nanoflowers (PNFs). The PNFs combined the function of both the enzyme and MRPs to realize biosensing through enzyme-mediated translation of the binding signal between MRPs and the target in solution.

The PNF material employing 15-PEP served as the foundation for the development of a CL bioassay technique for OTA. The PNFs, as depicted in Figure 3a, were fabricated with the self-assembly of 15-PEP and HRP in a calcium ion-containing phosphate buffer solution. Notably, this self-assembly process does not necessitate the use of organic solvents or rigorous reaction conditions, thereby preserving the enzymatic and MRP activity. Accordingly, a specific enhanced CL biosensor for OTA was successfully developed (Figure 3b), benefiting from the specific binding affinity between OTA and 15-PEP in PNFs.

The morphology of the nanoflowers was initially characterized using scanning electron microscopy (SEM) and transmission electron microscopy (TEM). Figures 3d–f and S10 illustrate that the petal-shaped spherical structure of PNFs has a diameter of about $2 \mu\text{m}$. The surface of the material consists of sheetlike “petal” structures, which exhibit a curled and ultrathin nature, as depicted in the locally enlarged images in Figure 3e. This characteristic is further confirmed by the TEM image shown in Figure 3f. During the growing process,

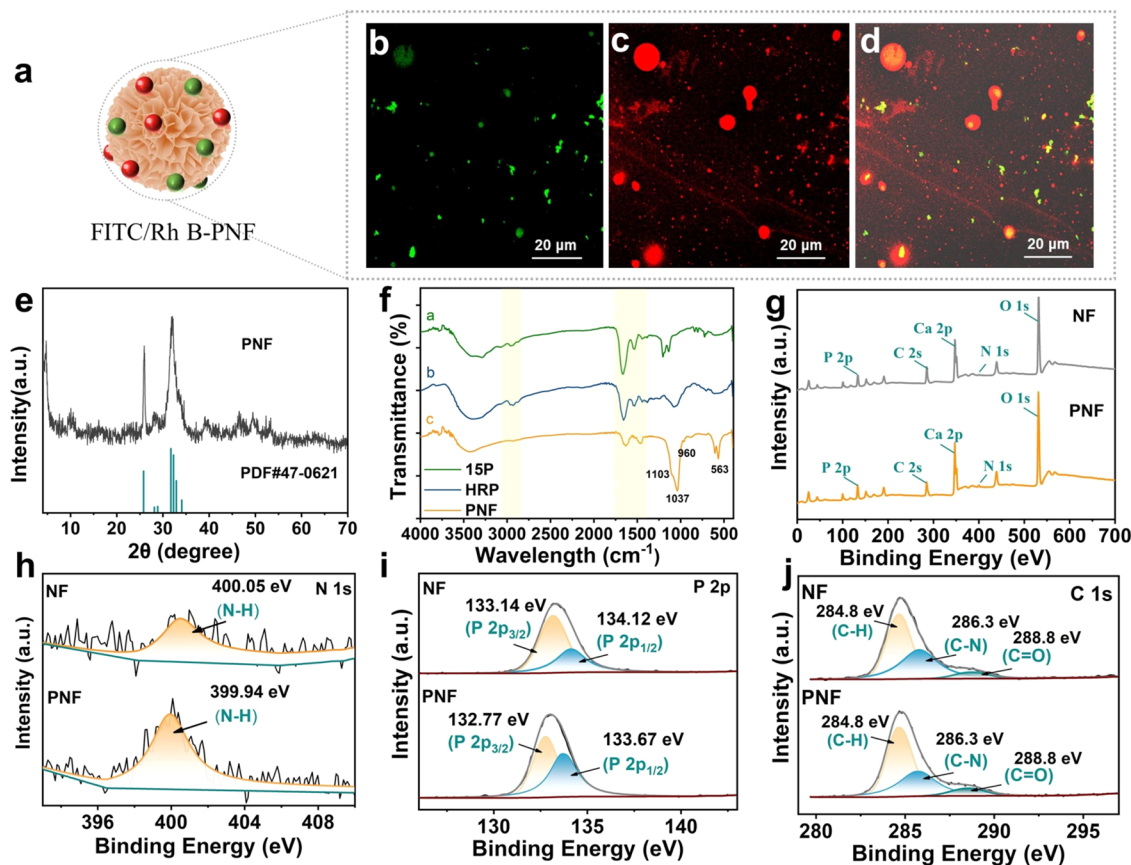


Figure 4. (a) Schematic diagram of the Rh B-labeled MRPs and FITC-labeled HRP to synthesize PNFs as usual. (b, c) Laser confocal fluorescence micrographs of PNFs with FITC-labeled HRP and Rh B-labeled 15-PEP. (d) XRD pattern and (e) FT-IR spectra of PNFs. (f) XPS survey spectra and (g) narrow scan spectra of (h) N 1s, (i) P 2p, and (j) C 1s of PNFs and NFs.

the kinetically controlled growth of calcium phosphate crystals originates at the individual Ca^{2+} -binding sites on the surfaces of the agglomerates (primary crystals), causing separate petals to appear (Figure 3d). In the final growth stage, the protein and peptide induce the nucleation of the calcium phosphate crystals to form the scaffold for the petals and serve as a “glue” to bind the petals together.^{30,37} The presence of peptides reduces the size of clumps formed by primary crystals and organic components, making them easier to nucleate independently. In contrast, without peptides, larger sheet-like crystal nanoflowers will form (Figure 3c). To confirm the immobilization of MRPs and protein in PNFs, a pretreatment was conducted on 15-PEP and HRP using rhodamine B (Rh B) and fluorescein isothiocyanate (FITC) (Figure 4a). Subsequently, fluorescence confocal microscopy images were obtained and are presented in Figure 4b–d. The material exhibited red and green fluorescence, attributed to the labeling of 15-PEP with Rh B and HRP with FITC, respectively, under excitation wavelengths of 561 and 488 nm. This compellingly supports the successful immobilization of both 15-PEP and HRP on the PNFs.

The element analysis of PNFs was explored through X-ray diffraction (XRD), Fourier transform infrared (FT-IR) spectroscopy, and X-ray photoelectron spectroscopy (XPS) analyses. The XRD data presented in Figure 4e demonstrate the presence of the inorganic constituent in the self-assembly hybrid nanoflowers, indicating a well-crystallized structure. This observation is matched well with the standard card of 47-0621 obtained from JCPDS from both positions and relative

intensities of diffraction peaks.³⁸ As shown in Figure 4f, FT-IR spectroscopy shows the stretching vibration of P–O and P=O (PO_4^{3-}) at 1103, 1037, 960, 565, and 563 cm^{-1} appearing in PNFs compared to 15-PEP and HRP. Specifically, 1103 and 1037 cm^{-1} are the asymmetric stretching vibrations of the phosphate group, 960 cm^{-1} is the symmetric stretching vibration, and 563 and 565 cm^{-1} are the in-plane bending vibrations. And the typical bands of protein (1400–1700 cm^{-1} for –CONH, 2962 and 3100 cm^{-1} attributed to – CH_2 and – CH_3) were observed in all of them. The O–H stretching peaks at 3200–3600 cm^{-1} come from the water molecules in the sample. Besides that, PNFs do not show a new characteristic peak and an obvious peak shift, demonstrating that there are no covalent bonds generated and indicating that the hybrid nanoflowers were formed via self-assembly.³¹

The surface chemistry and electronic structure of NFs and PNFs were studied by using XPS. The main elements found from the hybrid nanoflowers are C, O, P, Ca, and N (Figure 4g), suggesting calcium phosphate–peptide and protein complex formation. Compared with NFs, PNFs exhibit a notably increased intensity of N–H bonds (Figure 4h). Given that the sole difference between PNFs and NFs lies in the inclusion of peptides during the self-assembly, it can be inferred that the enhanced N–H bond strength on the surface of PNFs primarily stems from 15-PEP. This observation further indicates the abundant presence of peptides on the surface of the nanomaterials, with these increased N–H bonds originating primarily from the R-groups of the 15-PEP side chains, such as amino acids like lysine, leucine, glutamine,

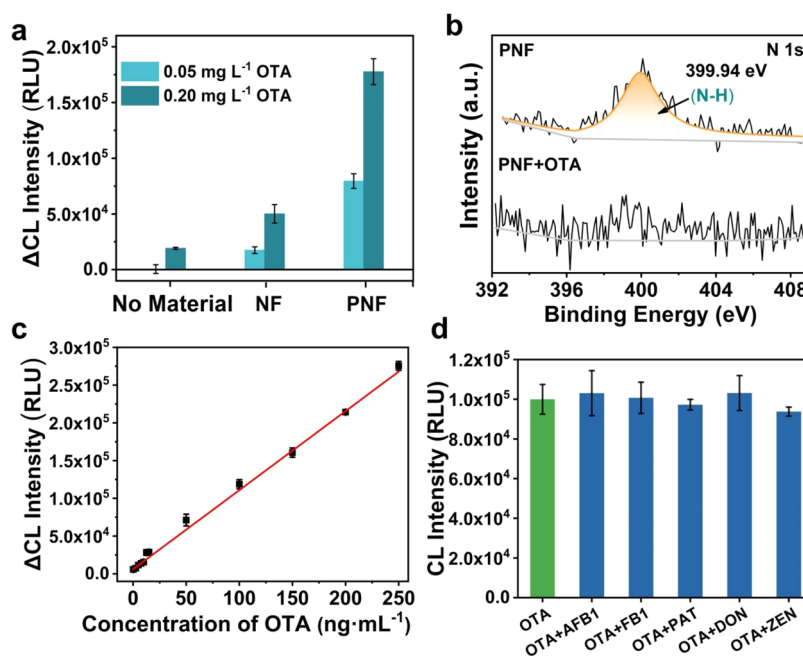


Figure 5. (a) Enhanced effect on different concentrations of OTA (0.05/0.20 mg·L⁻¹) for luminol/H₂O₂ in the absence of material and presence of NFs and PNFs. (b) XPS of the N 1 s spectrum of the comparison of PNFs and PNFs with OTA. (c) Linear fit of the calibration curves for OTA based on the ΔCL intensity. (d) CL intensity when OTA (1.0 ng·mL⁻¹) coexists with AFB₁ (5.0 ng·mL⁻¹), FB₁ (5.0 ng·mL⁻¹), PAT (5.0 ng·mL⁻¹), DON (5.0 ng·mL⁻¹), and ZEN (5.0 ng·mL⁻¹) in the PNFs catalyzing biosensing.

arginine, and phenylalanine. The carbon 1 s high-resolution XPS spectrum shown in Figure 4j can be deconvoluted into three characteristic features of hydrocarbon C–H bonding (284.8 eV), C–N bonding which is also true for N–C=O species (286.3 eV), and C=O bonding (288.8 eV).^{39,40} These results demonstrate that the successfully self-assembled PNF materials included HRP and 15-PEP with the calcium phosphate crystal, and the PNFs contain more characteristic residues from 15-PEP in the surface of the crystal material. The other supplementary data of XPS are shown in Figure S11, and the particle size distribution of nanoflowers is shown in Figure S12.

Enzyme-Peptide Self-Assembly Strategy for Detection of OTA. The mechanism of the HRP-catalyzed CL oxidation of luminol by H₂O₂ in the presence of high concentrations of OTA can be compared to the mechanism of *p*-iodophenol and other *p*-phenol derivatives that enhance CL. It is assumed that the generation of the phenoxy radical affects the CL intensity through the rate of enzyme turnover and the electron transfer between radicals and luminol.^{41–43} OTA was present in the form of monoanionic (OTA⁻) and dianionic (OTA²⁻) forms, which contained a phenoxy structure in the alkaline detection solutions. However, high concentrations of the phenoxy group are required to effectively enhance the conversion rate of enzymes and stabilize free radicals.

As shown in Figure 5a, even without HRP present, the phenoxy group in OTA (up to 0.2 mg·L⁻¹, about 200 times the limitation) can catalyze the CL reaction between H₂O₂ and luminol. When we added the synthesized organic–inorganic hybrid nanoflowers (NFs), which mainly consist of HRP and calcium ions, to the system, the NFs that act as fixed HRP enzymes rapidly catalyzed the luminol–H₂O₂ system. Similarly, the addition of OTA (phenoxy) enhances the catalyzed luminescence reaction significantly. At this point, the enhance-

ment of the catalyzed reaction is not exclusive to OTA, as it can also be enhanced by toxins with similar phenoxy structures, such as AFB₁, as shown in Figure S13. Finally, and most notably, the addition of enzyme-peptide nanoflowers (PNFs), consisting of HRP, calcium ions, and the most important MRPs, revealed that only OTA, even at concentrations as low as ppb, had the ability to significantly amplify the luminescence signal within the system. The detection limit for OTA was reduced by more than 200 times compared to the initial. What's more, in the presence of PNFs, even the extremely high concentration of AFB₁ (0.2 mg·L⁻¹) only has an enhancement effect similar to that of the NFs present. This suggests that the PNFs, owing to the inclusion of MRPs, possess the capability to specifically recognize and bind to OTA, thereby enabling highly selective detection. Furthermore, the 3D spherical architecture of the PNFs offers a substantial increase in the specific surface area, facilitating the efficient loading of target molecules.⁴⁴ Consequently, the enhanced signal amplification capability of these PNFs enables the detection of OTA at even lower concentrations. This evidence demonstrated that PNFs could transduce and amplify the enhanced luminescence of OTA in the luminol–H₂O₂ system.

To further investigate the binding mechanism of MRPs in PNFs toward OTA, XPS characterizations were performed to analyze the interaction between PNFs and OTA (Figure S14). The most significant difference was observed in the N 1 s spectrum. Compared to PNFs with an obviously N–H bond at 399.94 eV, it was not found in the mixture of PNFs with OTA. Based on the previous experiment, we can see the N–H bond is mainly from 15-PEP (Figure 4g); thus, the disappearance of the peak for N–H illustrates 15-PEP binding to OTA directly (Figure 5b). The tested zeta potential shown in Figure S15 illustrates that the surface charges of PNFs and OTA display opposite charges,⁴⁵ respectively, which is beneficial for electrostatic attraction between PNFs and OTA.

Under optimal assay conditions (Figure S16–S19), we investigated the enhanced CL intensity associated with PNFs in the presence of various concentrations of OTA. A standard curve generated by plotting the ΔCL value (Figure 5c) illustrated a linear working range of 0.24–250 ng·mL⁻¹ and the linear regression equation was $\Delta\text{CL} = 1046 C_{\text{OTA}} + 6189$ ($R^2 = 0.99$), and the limit of detection (LOD) was 0.08 ng·mL⁻¹ ($3.3\sigma/S$) and the limit of quantitation (LOQ) was 0.24 ng·mL⁻¹ ($10\sigma/S$). Compared to previous reports, especially immunosensors, the developed enhanced CL method shows comparable or lower LODs and linear ranges (Table S2). To verify the selectivity of the enhanced CL assay, we investigate its ability to recognize OTA in the presence of other mycotoxins, including AFB1, FB1, PAT, DON, and ZEN. The developed bioassay exhibits high specificity, as evidenced by the absence of significant interference from other mycotoxins (Figures 5d and S20), identical with the results obtained from the previous MD simulations (Figure S6). In addition, the stability of the prepared PNF material was evaluated by storing it at -20 °C for 30 days (Figure S21).

Practical Application in the Grain and Beer Samples.

The developed enhanced CL biosensing was validated by analyzing a quality control sample (Pribolab, MRM-OW-50) of wheat flour for OTA. The determined concentration of OTA in MRM-OW-50, utilizing the enhanced CL bioassay, was $11.80 \pm 0.70 \mu\text{g}\cdot\text{kg}^{-1}$ ($n = 3$), which closely aligns with the certified value of $12.21 \mu\text{g}\cdot\text{kg}^{-1}$, thereby attesting to the accuracy of the developed method. We subsequently employed the developed bioassay to assess the OTA concentration in four grain and beer samples. The analytical outcomes are summarized in Table S3. The determined OTA levels in oats and yellow maize samples were below the LOQ (0.24 ng·mL⁻¹), and the concentration in corn grit was $1.92 \pm 0.42 \mu\text{g}\cdot\text{kg}^{-1}$, remaining well within the maximum permissible limit established by the Codex Alimentarius Commission (CAC) ($5 \mu\text{g}\cdot\text{kg}^{-1}$) (Mycotoxins, WHO, 2019). The recoveries of OTA spiked into the grain samples were in the range of 107.6–118.0%. The developed biosensor was validated using the HPLC method (Table S3). These results show that the proposed method is reliable for detecting OTA in actual samples.

CONCLUSIONS

This study presents a computational design approach that employs a top-down methodology to obtain MRPs for toxic and low-immunity small molecules. As a proof-of-concept, a 15-mer peptide was designed from the HSA subdomain for OTA. Through molecular dynamics simulations, it was observed that this MRP exhibited specific binding to OTA while displaying minimal or no affinity toward other structurally similar mycotoxins. Subsequently, we successfully synthesized novel enzyme-peptide self-assembly hybrid nanoflowers known as PNFs, capable of generating a signal probe without the need for chemical modification or coupling reactions. Furthermore, we developed an enhanced CL biosensing for OTA using PNFs, which exhibited a rapid, simple, and highly sensitive performance with a low detection limit of 0.08 ng·mL⁻¹ and a wide detection range of 0.24–250 ng·mL⁻¹. The design of the peptide and the peptide-based rapid detection method hold promise for future bioassays. More importantly, the possibility of MRPs as recognition receptors in the rapid detection of small molecules was

explored, particularly for small molecules that are challenging to target with antibodies.

ASSOCIATED CONTENT

Supporting Information

The Supporting Information is available free of charge at <https://pubs.acs.org/doi/10.1021/acs.analchem.4c04295>.

Additional simulation details; apparatus and instruments; the sequence of peptides; additional simulation data; synthesis and characterization of OTA-BSA and XPS spectra of nanoflowers; the size of nanoflowers modulated by the concentration, composition ratio, or incubating time; zeta potential of PNFs and OTA; synthesis optimization; detection condition optimization; storage stability of PNFs; sensitivity comparison with antibody and aptamer sensors for OTA detection; and determination of OTA in grain and beer samples (PDF)

AUTHOR INFORMATION

Corresponding Author

Xiaofang Shen – School of Food Science and Technology, Jiangnan University, Wuxi 214122, People's Republic of China; orcid.org/0000-0002-3929-9228; Email: xfshen@jiangnan.edu.cn

Authors

Lihong Yu – School of Food Science and Technology, Jiangnan University, Wuxi 214122, People's Republic of China

Chenglin Yang – School of Food Science and Technology, Jiangnan University, Wuxi 214122, People's Republic of China

Shuting Cheng – School of Food Science and Technology, Jiangnan University, Wuxi 214122, People's Republic of China

Qianqian Jiang – School of Food Science and Technology, Jiangnan University, Wuxi 214122, People's Republic of China

Yuehong Pang – School of Food Science and Technology, Jiangnan University, Wuxi 214122, People's Republic of China; orcid.org/0000-0002-8050-7375

Complete contact information is available at:

<https://pubs.acs.org/doi/10.1021/acs.analchem.4c04295>

Notes

The authors declare no competing financial interest.

ACKNOWLEDGMENTS

We greatly appreciate the financial support from the National Natural Science Foundation of China (22476068, 22076067).

REFERENCES

- (1) Yu, H.; Alkhamis, O.; Canoura, J.; Liu, Y.; Xiao, Y. *Angew. Chem., Int. Ed.* **2021**, *60* (31), 16800–16823.
- (2) Liang, M.; Li, Z.; Wang, W.; Liu, J.; Liu, L.; Zhu, G.; Karthik, L.; Wang, M.; Wang, K.-F.; Wang, Z.; et al. *Nat. Commun.* **2019**, *10*, No. 3672.
- (3) Pedroso, C. C. S.; Mann, V. R.; Zuberbuhler, K.; Bohn, M.-F.; Yu, J.; Altoe, V.; Craik, C. S.; Cohen, B. E. *ACS Nano* **2021**, *15* (11), 18374–18384.
- (4) Pundir, M.; Papagerakis, S.; De Rosa, M. C.; Chronis, N.; Kurabayashi, K.; Abdulmawjood, S.; Prince, M. E. P.; Lobanova, L.; Chen, X.; Papagerakis, P. *Biotechnol. Adv.* **2022**, *59*, No. 107961.

- (5) Wei, Y.; Tao, Z.; Wan, L.; Zong, C.; Wu, J.; Tan, X.; Wang, B.; Guo, Z.; Zhang, L.; Yuan, H.; et al. *Biosens. Bioelectron.* **2022**, *211*, No. 114282.
- (6) Alkhamis, O.; Canoura, J.; Yu, H.; Liu, Y.; Xiao, Y. *TrAC, Trends Anal. Chem.* **2019**, *121*, No. 115699.
- (7) Wu, L.; Wang, Y.; Xu, X.; Liu, Y.; Lin, B.; Zhang, M.; Zhang, J.; Wan, S.; Yang, C.; Tan, W. *Chem. Rev.* **2021**, *121* (19), 12035–12105.
- (8) Muchowska, K. B.; Muchowska, J. M. *Science* **2020**, *370* (6518), 767–768.
- (9) Schwieter, K. E.; Johnston, J. N. *J. Am. Chem. Soc.* **2016**, *138* (43), 14160–14169.
- (10) Giraudi, G.; Anfossi, L.; Baggiani, C.; Giovannoli, C.; Tozzi, C. *J. Chromatogr., A* **2007**, *1175* (2), 174–180.
- (11) Rahi, S.; Lanjekar, V.; Ghormade, V. *Food Control* **2022**, *136*, No. 108842, DOI: 10.1016/j.foodcont.2022.108842.
- (12) Dotter, H.; Boll, M.; Eder, M.; Eder, A.-C. *Biotechnol. Adv.* **2021**, *47*, No. 107699.
- (13) Huang, Y.; Wiedmann, M. M.; Suga, H. *Chem. Rev.* **2019**, *119* (17), 10360–10391.
- (14) Mimmi, S.; Maisano, D.; Quinto, I.; Iaccino, E. *Trends Pharmacol. Sci.* **2019**, *40* (2), 87–91.
- (15) Fu, H. J.; Chen, Z. J.; Wang, H.; Luo, L.; Wang, Y.; Huang, R. M.; Xu, Z. L.; Hammock, B. J. *Hazard. Mater.* **2021**, *406*, No. 124288.
- (16) Li, Y. K.; Wang, X. Y.; Liu, X.; Yang, T.; Chen, M. L.; Wang, J. H. *Analyst* **2020**, *145* (15), 5280–5288.
- (17) Kim, S. J.; Lee, Y.; Choi, E. J.; Lee, J. M.; Kim, K. H.; Oh, J. W. *Nano Convergence* **2023**, *10*, No. 1.
- (18) Yu, Y.; Xu, S.; He, R.; Liang, G. J. *Agric. Food Chem.* **2023**, *71*, 2684–2703.
- (19) Bhardwaj, G.; Mulligan, V. K.; Bahl, C. D.; Gilmore, J. M.; Harvey, P. J.; Cheneval, O.; Buchko, G. W.; Pulavarti, S. V. S. R. K.; Kaas, Q.; Eletsky, A.; et al. *Nature* **2016**, *538* (7625), 329–335.
- (20) Jefferson, R. E.; Oggier, A.; Füglistaler, A.; Camviel, N.; Hijazi, M.; Villarreal, A. R.; Arber, C.; Barth, P. *Nat. Commun.* **2023**, *14* (1), No. 2875.
- (21) Diller, D. J.; Swanson, J.; Bayden, A. S.; Jarosinski, M.; Audie, J. *Future Med. Chem.* **2015**, *7* (16), 2173–2193.
- (22) Blaber, M.; Lee, J. *Curr. Opin. Struct. Biol.* **2012**, *22* (4), 442–450.
- (23) Han, Y.; Král, P. *ACS Nano* **2020**, *14* (4), 5143–5147.
- (24) Gerasimov, J. Y.; Lai, R. Y. *Chem. Commun.* **2010**, *46* (3), 395–397.
- (25) Lock, L. L.; Reyes, C. D.; Zhang, P.; Cui, H. *J. Am. Chem. Soc.* **2016**, *138* (10), 3533–3540.
- (26) Ahn, S.; Lee, S.; Lee, J.; Kim, B. *Food Chem.* **2016**, *190*, 368–373.
- (27) Bazin, I.; Andreotti, N.; Hassine, A. I. H.; De Waard, M.; Sabatier, J. M.; Gonzalez, C. *Biosens. Bioelectron.* **2013**, *40* (1), 240–246.
- (28) Manna, S.; Maiti, S.; Shen, J.; Du, W.; Esser-Kahn, A. P. *ACS Cent. Sci.* **2020**, *6*, 2071–2078.
- (29) Xu, D.; Samways, D. S. K.; Dong, H. *Bioact. Mater.* **2017**, *2*, 260–268.
- (30) Ge, J.; Lei, J.; Zare, R. N. *Nat. Nanotechnol.* **2012**, *7* (7), 428–432.
- (31) Zhao, M.; Yao, X.; Li, J.; Hu, H.; Ren, J.; Xu, J.; Wang, J.; Zhang, D. *Biosens. Bioelectron.* **2023**, *230*, No. 115264.
- (32) Dai, J.; Park, G.; Perry, J. L.; Il'ichev, Y. V.; Bow, D. A. J.; Pritchard, J. B.; Faucet, V.; Pfohl-Leszkowicz, A.; Manderville, R. A.; Simon, J. D. *Acc. Chem. Res.* **2004**, *37* (11), 874–881.
- (33) Poór, M.; Kunsagi-Mate, S.; Czibulya, Z.; Li, Y.; Peles-Lemli, B.; Petrik, J.; Vladimir-Knezevic, S.; Koszegi, T. *Luminescence* **2013**, *28* (5), 726–733.
- (34) Studer-Rohr, I.; Schlatter, J.; Dietrich, D. R. *Arch. Toxicol.* **2000**, *74* (9), 499–510.
- (35) Faisal, Z.; Derdak, D.; Lemli, B.; Kunsagi-Mate, S.; Balint, M.; Hetenyi, C.; Csepregi, R.; Koszegi, T.; Sueck, F.; Cramer, B.; et al. *Toxins* **2018**, *10* (9), No. 353.
- (36) Adasme, M. F.; Linnemann, K. L.; Bolz, S. N.; Kaiser, F.; Salentin, S.; Haupt, V. J.; Schroeder, M. *Nucleic Acids Res.* **2021**, *49* (1), 530–534.
- (37) Chen, W.; Tian, R.; Xu, C.; Yung, B. C.; Wang, G.; Liu, Y.; Ni, Q.; Zhang, F.; Zhou, Z.; Wang, J.; et al. *Nat. Commun.* **2017**, *8* (1), No. 1777.
- (38) Hao, Y.; Li, H.; Cao, Y.; Chen, Y.; Lei, M.; Zhang, T.; Xiao, Y.; Chu, B.; Qian, Z. *J. Biomed. Nanotechnol.* **2019**, *15* (5), 951–965.
- (39) Ghosh, K.; Balog, E. R. M.; Sista, P.; Williams, D. J.; Kelly, D.; Martinez, J. S.; Rocha, R. C. *APL Mater.* **2014**, *2* (2), No. 021101.
- (40) Zhang, C.-Y.; Zhang, H.; Yang, F.-Q. *Microchem. J.* **2021**, *168*, No. 106489.
- (41) Dotsikas, Y.; Loukas, Y. *Talanta* **2007**, *71* (2), 906–910.
- (42) Liu, J.; Zhang, L.; Fu, C.; Wang, Y.; Sun, S. *Luminescence* **2015**, *30* (8), 1297–1302.
- (43) Wada, M.; Abe, K.; Ikeda, R.; Harada, S.; Kuroda, N.; Nakashima, K. *Talanta* **2010**, *81* (3), 1133–1136.
- (44) Park, W. M.; Champion, J. A. *ACS Nano* **2016**, *10* (9), 8271–8280.
- (45) Hagiya, K.; Miyagawa, A.; Nagatomo, S.; Nakatani, K. *Anal. Chem.* **2022**, *94* (16), 6304–6310.